www.sciencemag.org/content/349/6247/aab0639/suppl/DC1

# Supplementary Materials for

## Properties of the 67P/Churyumov-Gerasimenko interior revealed by CONSERT radar

Wlodek Kofman,* Alain Herique, Yves Barbin, Jean-Pierre Barriot, Valérie Ciarletti, Stephen Clifford, Peter Edenhofer, Charles Elachi, Christelle Eyraud, Jean-Pierre Goutail, Essam Heggy, Laurent Jorda, Jérémie Lasue, Anny-Chantal Levasseur-Regourd, Erling Nielsen, Pierre Pasquero, Frank Preusker, Pascal Puget, Dirk Plettemeier, Yves Rogez, Holger Sierks, Christoph Statz, Hakan Svedhem, Iwan Williams, Sonia Zine, Jakob Van Zyln

*Corresponding author. E-mail: wlodek.kofman@obs.ujf-grenoble.fr

Published 31 July 2015, *Science* **349**, aab0639 (2015)
DOI: 10.1126/science.aab0639

**This PDF file includes:**

# Materials and methods

## CONSERT Experiment

System

The CONSERT instrument is a bistatic radar which consists of two separate units: The Lander CONSERT unit (LCN) located on Philae and the Orbiter CONSERT unit (OCN) located on the orbiter.

Each unit is composed of a transmitter, receiver and control unit (*5,29,30*) as well as a wide beam (78°) antenna (*31*) on both lander and orbiter. The transmitted signal is a 90 MHz electromagnetic modulated wave; the transmitters and receivers on Philae and Rosetta are almost identical. Rosetta transmits the signal to Philae, where the signal is processed. The arrival time of the strongest received signal is detected and the new signal, synchronized on the arriving time, is sent back to Rosetta. The first transmission synchronizes CONSERT on Rosetta and Philae, while the returned signal is used for science measurements. The received signals are stored and send to the Earth. All these operations are made on the 300 ms time scale (*5, 29*). This fast operation ensures that the signal propagates along the same paths both to and from Philae since neither will have moved significantly in such a short time interval. The received signal contains the information about the interior of the comet and its dielectric properties. The temporal form of the signal contains also important information about its volume and surface scattering and about the homogeneity of the penetrated material. The signal frequency bandwidth is 10 MHz, providing a spatial resolution of about 30m (100ns) in the free space. The accuracy of the propagation time measurements is of the order of 10-15 ns (about 3-5 m in the free space) for the large signal-to-noise ratio (SNR) above 20 dB. The absolute time calibration requires knowledge of the system delay and frequency drift, and these depend strongly on environmental conditions such as temperature. We estimate that the absolute time accuracy gives measured distance accuracy of the order of 10m.

When the SNR is good, the radiometric accuracy on the amplitude measurements is better than 2 dB (not taking into account antenna and polarization). However the fine interpretation of the variability as a function of the relative positions of Philae and Rosetta remains difficult at this stage, with Philae exact position as well as its attitude and antenna position relative to the surface still unknown. These missing pieces of information are needed to model properly the antenna gain and polarization, and therefore to perform an accurate analysis of the measured amplitude. To do this, knowledge of the close environment of Philae is needed, which may become possible at a later stage whenever Philae is located.

Data

All the data were analyzed and the propagation time between Philae and Rosetta was measured. Signals were processed by a matched filter that takes into account the receiver filters and system delays. Signals were adequately processed to increase the accuracy of the arrival time measurements (10-15 ns). Figure 4 shows the measured propagation time between Philae and Rosetta as function of observation time. The delays for the strongest peaks in signal (down to a level -6dB below the strongest one) are shown. For most

soundings, there is one detected signal peak corresponding to a single propagation path. Sometimes two or three paths are seen.

The quality of the CONSERT data has been assessed according to the (SNR) obtained at both the Philae (LCN) and Rosetta (OCN) CONSERT instruments. Four different classes of quality level have been identified (see Table S1).
The results during the First Science Sequence (FSS) are summarized in Table S2 as a function of the observation time.
The ground tracks of the different sequences of measurements are visualized on the nucleus 3D shape model in Fig.1, S1 and S2. For each sounding, the intersection of the straight line between Philae and Rosetta, and the nucleus shape model is indicated by a coloured dot. The colour code gives the corresponding class of signal quality given in Table S2.
As seen from Table S2 and Figures S1 and S2, the SNR was, at times, too low for the detection (class 4) or synchronization (class 2, 3) of a signal between the Philae and Rosetta components of CONSERT. This lack of communication can be explained by the combination of several adverse conditions during the FSS, namely:

- The FSS orbit was not well suited for the CONSERT measurements,
- The lander antenna was not well positioned with respect to the surface, resulting in low gain of antenna and a polarization mismatch between Rosetta and Philae, and
- The observed noise level on Philae was much larger (about 12dB) during FSS than during the cruise, partly blinding the transponder.

In addition, the absorption and/or scattering of the signal inside the comet may have contributed to the lack of detection. This conclusion is supported by the fact that the loss of the signal coincided with the times that the signal between Philae and Rosetta had to propagate through the greatest thickness of the nucleus (i.e., when the positions of the spacecraft were nearly antipodal to one another).
Therefore, only the data corresponding to signal class 1 have been considered in the paper. In Figure S3 multiple echoes are visible in both data sets, especially in Figure S3A before 19h10 UTC. Further analysis is needed to explain these results but the short duration of each echo rules out any significant scattering inside the nucleus.

**Simulations and dielectric properties of the comet deduced from the CONSERT data**

The 3D simulation uses a ray-tracing algorithm valid, through a slowly variable dielectric medium. The optical path is integrated using the WKB method. Sharp variations of the dielectric constant are modeled by interfaces between media of different dielectric properties, using either parametric equations, or triangular meshes. We use the Fresnel refraction's law to compute the propagation through these interfaces. We calculated also the amplitude of the propagating signal solving the transport equation.
As the exact position of the Philae is not known, we have run simulations assuming 243 hypothetical landing sites separated by 5m inside the strip defined by CONSERT

triangulation measurements (*6)*. This strip has been extended in the simulation to see how large the potential landing site area is.

In Fig. S4 we present the results globalizing our simulations corresponding to the measurements performed during the FSS in the evening and in the morning. Each dot represents a potential location for the lander that has been considered for the simulations. For each location, the dot's color shows the permitivity value that leads to the best match between measured and simulated delay for the main path. When no acceptable match is found, the dot has no color. The dimension of the dots gives a confidence index for the evaluation of this permittivity value. For each landing site, the root mean square error (R.M.S.) between experimental and simulated propagation delays for all the measurements orbital points is computed. The best match is obtained for the permittivity value that gives the lowest R.M.S. (see Fig. S5) and the confidence index is proportional to the inverse of this minimum R.M.S value. In order to account for the fact that we are looking for a permittivity value that gives a good match for the whole set of experimental data, we normalized the R.M.S. value by the square root of the ratio between the number of orbital points that actually receive a simulated signal and the total number of orbital points of the considered period (evening or morning). Therefore, the bigger the circle, the better the result.
Fig. S4 maps show that some landing sites offer no solution: tiny west area for the evening set of data and a wide east part for the morning one. The analysis of the evening and morning sectors shows also that when one obtains permittivity close to 1.35 in the evening, for a given landing site, then in the morning the obtained permittivity is close to 1.05. This would indicate that there is large difference in porosity or in composition between the west part and the east part of the head of the comet. There is no geomorphological evidence for this kind of conclusion. Since the landing site is unique these locations can all be excluded from the set of acceptable locations for the lander. In addition, some of the investigated sites would require very low dielectric constant value (1.05-1.1, blue color) which is very close to the free space permittivity value that we believe is not realistic in the cometary nucleus. Assuming that the average permittivity value must be in the same range for the two sets of measurements that both sounded the smaller lobe of the nucleus, we identify a limited number of landing site locations that are physically acceptable.
Fig S5 illustrates the method for a set of 10 possible Philae locations. Each curve corresponds to a site (labelled A, B, …, I) which localization is shown in the upper rigth map of Fig. S5. The R.M.S. value are in μs (0.1μs corresponding to 30 m in free space). The best estimate of the relative permittivity value is obtained for the smallest value of the R.M.S. The figures show that the best consistency between the evening and morning sets of values, is highlighted by the ticker curve and corresponds to a permittivity value of 1.275 and to landing site D.

Our method allows us to get simultaneously our best estimate of both Philae location and the mean permittivity value inside the small lobe of the nucleus sounded by CONSERT.
The fact that the R.M.S minimum moves from site A to J for the evening and morning measurements, and reaches the minimum for permittivity 1.22 – 1.32 helps to identify

this possible landing area. A similar analysis was performed with the geographical orthogonal axis (not shown in Fig.S5).
In the Fig. 5 of the main article we show this area and the overall best fit.

**The interpretation of permittivity measurements**

Effective permittivity
In order to retrieve the bulk nucleus permittivity estimated from CONSERT, the effective permittivity of various ice and dust mixtures with different porosities is calculated using mixing formulas, with assumptions regarding the dust and ice composition. This gives a range of ice and dust volume fraction compatible with the CONSERT estimation of the mean permittivity. This domain is drawn on a ternary diagram (*28*) while the values are summarized in the Table S3. To calculate effective permittivity, we use Hashin-Shtrikman bounds *(13*) with lab measurements of meteoritic material (*18*).

Dust Fraction
As well as the icy component of the comet material, which primarily consists of $H_2O$, CO and $CO_2$ molecules, the non-icy component also plays a significant role in modifying the dielectric properties of the cometary mixture.
Ground-based observations suggest that most cometary dust is an unequilibrated, heterogeneous mixture of crystalline and glassy silicate minerals, organic refractory material, and other constituents such as iron sulfide and FeNi metal (*23* and references therein).
The mean elemental composition of samples collected by Stardust in the coma of comet Wild 2 suggests a CI-like composition consistent with the bulk solar system composition for primitive material *(24, 25, 26).* They appear primarily constituted of ferromagnesian silicates, Fe-Ni and Fe-Ni metal. Abundant amorphous silicates were also detected in addition to the crystalline silicates, consistent with mixing of solar system and interstellar matter. The accreted material could include Al-rich and Si-rich chondrule fragments together with some CAI-like fragments. These materials, combined with fine-grained components in the tracks, may be assumed to be analogous to components in unequilibrated chondritic meteorites and to aggregates observed in some interplanetary dust particles collected in the Earth stratosphere (IDPs, *27*).
Therefore, potential analogue meteoritic material for comparison with cometary dust includes the ordinary and the carbonaceous chondrites groups.
Analysis of the Stardust tracks in aerogel and impacts on foils establishes that the typical size range of dust particles is between 5 and 25 μm. A mixture of compact and cohesive grains (65%) and friable less cohesive aggregated structures (35%) is noticed, with constituent grains of a size below 1 μm and a size distribution consistent with measurements in the comae of comets *(32, 33).* This aggregated structure at the micrometer scale has been recently confirmed for 67P/C-G by the COSIMA imaging (*12*).
Organics found in samples from comet 81P/Wild 2 present a heterogeneous and unequilibrated distribution in both abundance and composition. It suggests that amorphous carbon and organic carbon are dominant *(34).* Overall, more than two dozen

organic parent molecules (possibly including glycine) have been identified and are responsible for much of the coma chemistry taking place around comets, indicating the variety and complexity of the organic content of those bodies (35 and references therein). Such a variety of composition is beginning to be identified in 67P/C-G for which VIRTIS has shown spectral features consistent with opaque minerals associated with nonvolatile organic macromolecular materials: a complex mixture of various types of carbon-hydrogen and/or oxygen-hydrogen chemical groups, with little contribution of nitrogen-hydrogen groups (*11*)

As parameters to be inserted into the mixing formula, two types of chondritic meteorites were considered. The first are two ordinary chondrites (OC) and the second are two carbonaceous chondrites (CC). The laboratory-measured dielectric constants are used as parameters to calculate the volume of dust to ice ratio using the dielectric mixing formulas. Hence we constrain the ambiguity associated with the value of the dust to ice ratio for the head of the comet by using a dielectric mixture of the two most common set of materials to be encountered on 67P/C-G, that is porous ice and chondritic dust.

For the ordinary chondrites, we consider laboratory permittivity measurement on meteoritic samples from the NASA Johnson Space Center Curation office for the U.S. Antarctic Meteorite Collection. In particular we use low iron content chondrites, the L5 (Meteorite Hills (MET) 01260) and the LL5 (MacAlpine Hills (MAC) 88122). The values of the permittivity of the two desiccated samples in the 10 to 100 MHz frequency band and at a temperature of 130 K are respectively 5.6 and 4.7 (*18*). For the carbonaceous chondrites, we take the laboratory measured permittivity on the desiccated CR2 (NWA 801) and CM (NWA 5797) meteoritic class samples. Both CR2 and CM samples were analyzed in the laboratory and measurements are shown in Fig. S6. In our calculations will use permittivity values of 2.6 and 2.9 respectively in the 10 to 100 MHz frequency band at 130 K.

For the two chondritic sample sets, we measure the permittivity on dust compacted pellets. The porosity in the pellets was measured at ~30% using a mercury porosimeter. Hence, the dust fraction derived from the CONSERT measurement includes this 30% micro-porosity. In the ternary diagram we consider total porosity (micro- and macro-porosity) versus ice and dust material without any porosity. To normalize for the pellets porosity, the estimated dust fraction has been split in two parts: the grain dust fraction equal 0.7 times the estimated dust fraction and corresponding to the fraction of material without any porosity and the porosity part of the experimental sample equals 0.3 times the estimated dust fraction which has been added to the total porosity. The materials used and their dielectric properties from Hashin-Shtrikman bounds are shown in the Table S3. In the table value of 3.1 for permittivity for amorphous ice are is used in calculations of dielectric mixture with $CO_2$ ice in order obtain the lower bound of ice ratio. The upper limit is calculated with permittivity 3.1 for the water ice. Using 3.4 for permittivity of amorphous ice will change the bounds of about 1.8% as it can be seen in the table. The use of 3.4 will not change the final conclusion as the dust to ice ratio limits possible values in this area of the ternary graph (Fig. S9 and Table S5).

In the ternary diagram (Fig. S7) we plotted the constraints indicated in the Table S3 for OC (yellow) and CC (red), and the green and blue lines defined by the dust/ice ratio and the density constraints (Fig. S8, Table S4).

Density values

Based on measurements performed by Rosetta, 67P/C-G has a mass of $1.0 \times 10^{13}$ kg.
Using this mass and the volume determined by the OSIRIS investigation, a bulk density of 470 +/- 45 kg $m^{-3}$ was calculated (*8*).
This bulk density is only consistent with a specific area in the ternary diagram between pure ice, pure dust and 100% porosity material. Assuming that ice is principally constituted of the mixture of the $H_2O$, CO and $CO_2$ with the water ice density of 917 $kg.m^{-3}$ and the mixture density of 1078 $kg.m^{-3}$, for the latter value we have taken the $H_2O$/ $CO_2$ mixture (75%/25%).
Regarding the dust density, a number of values have been suggested but they often do not take into consideration the effect of microporosity in reducing the bulk density of dust particles. We are primarily interested in the value of compact material. The recent direct measurements taken by the Rosetta spacecraft around 67P/C-G using GIADA (Grain Impact Analyzer and Dust Accumulator), would constrain the bulk density to ($1.9 \pm 1.1 \times 10^3$ kg $m^{-3}$), assuming spherical grains (*36*). These values should include the effect of the microporosity of the dust, which is known to be high from the COSIMA measurements (*12*).
The large compilation of grain density, bulk density and porosity measured on the collection of meteorites in (*37*) allow us to separate the above-mentioned effect from porosity. The grain density (defined to be the density of the material constituting the meteorite without the porosity) of several meteorites can be used to constrain the density of grains relevant to comets. The ordinary chondrites L and LL groups have a grain density of about 3500 kg $m^{-3}$, the carbonaceous chondrites CI have a grain density of about 2500 kg $m^{-3}$, and the carbonaceous chondrites CM have a grain density of about 2900 kg $m^{-3}$.
It is interesting to note that laboratory analysis of the 81P/Wild 2 samples returned by the Stardust mission showed their mean elemental composition to be similar to a CI-like composition consistent with a bulk solar system composition for primitive material (*24, 25, 26*).
As a conclusion, it may be assumed, in a first approach, the grain density of dust from 67P/C-G to range from 2500 to 3500 kg $m^{-3}$. Table S4 shows the ice and dust fractions as function of measured average density of the comet and assumed grain density.

Dust to ice ratio

One of the most important properties of a comet is the dust to ice mass ratio, as it clearly distinguishes between the behavior of various comets (*38*).
The values that are obtained from comet observations depend on a number of assumptions regarding the grain distribution and density and the physical properties of the comet. For 67P/C-G, the dust to ice mass ratio has been determined from ground based observations to range from relatively low values of 0.5 to 1.75 (*39, 40*) to higher values 3 to 4.8 (*41, 42*).

A combination of measurements taken by the Rosetta spacecraft with the GIADA and OSIRIS instruments for dust detection, and the MIRO and ROSINA instruments for the gas emitted by the comet suggests that the current dust/gas mass ratio of 67P/C-G is 4 +/- 2 averaged over the sunlit nucleus surface (*34*) confirming the relative dusty nature of the comet. However, it must be remembered that this measurement during the low activity period of the comet is unlikely to reflect the bulk dust to gas mass ratio of the comet nucleus and may vary during the whole lifetime of the mission.

The Table S5 below summarizes the range of values for the dust to ice volumetric ratio obtained from the ground-based observations and the measurements of Rosetta. Fig. S9 shows the ternary diagram for dust/ice limits.

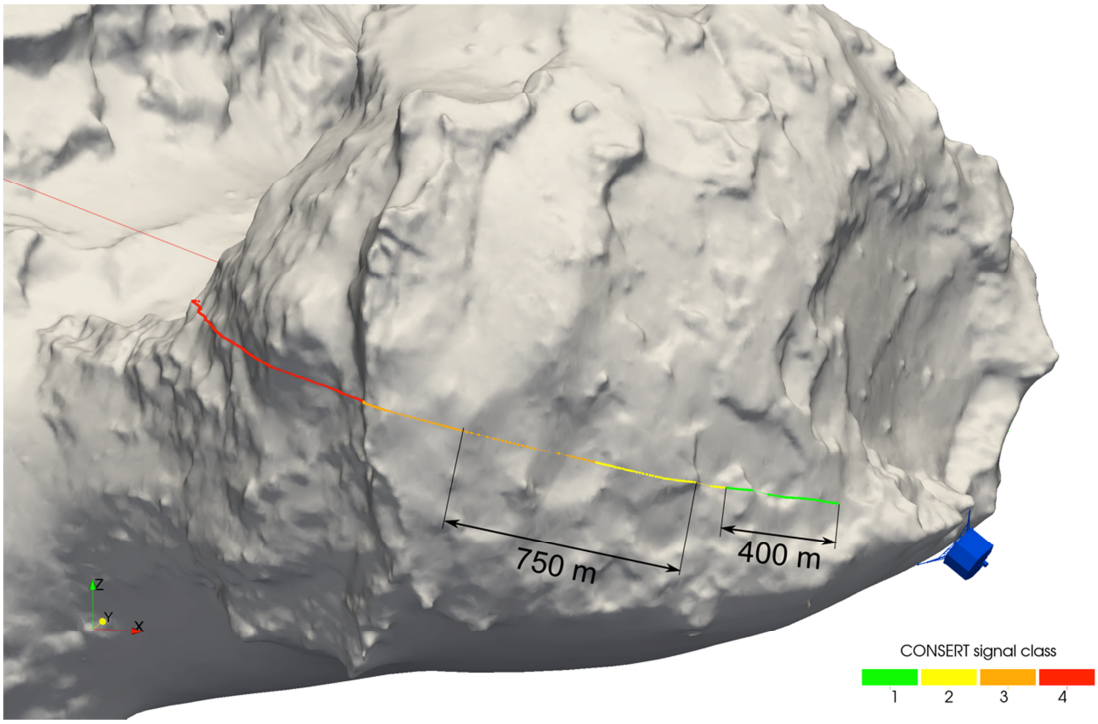


**Fig. S1**

Ground track for the first sequences of measurements in the evening of Nov. 12 (West part of the head)

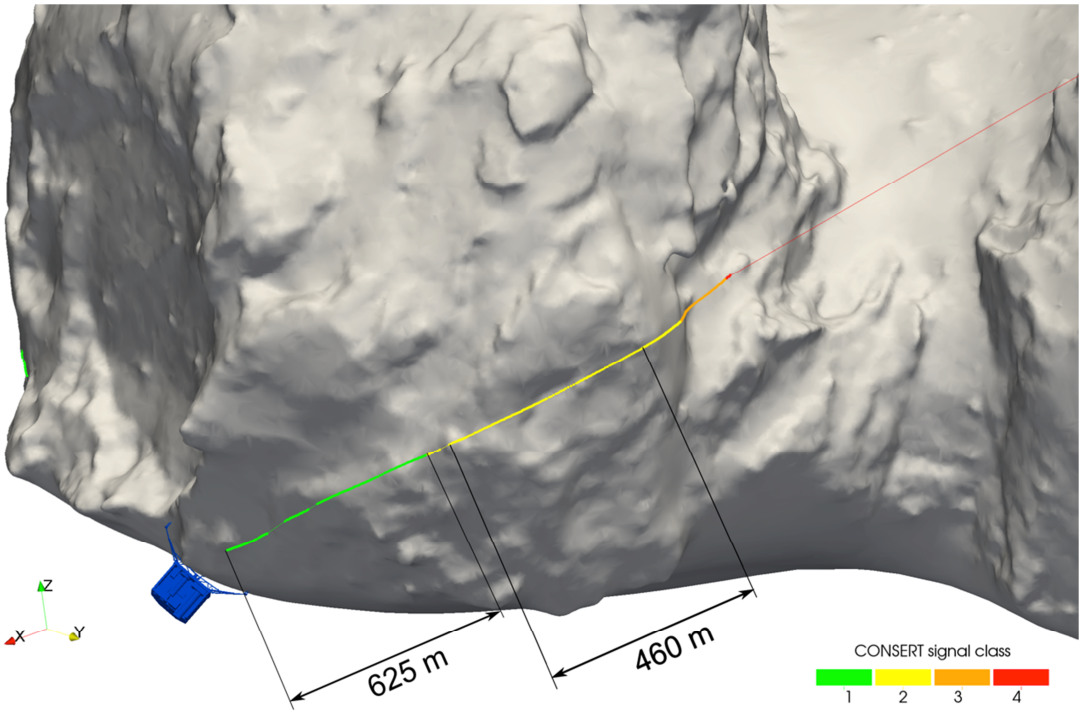


**Fig. S2**

Ground track for the last sequence of measurements in the morning of Nov. 13 (East part of the head).

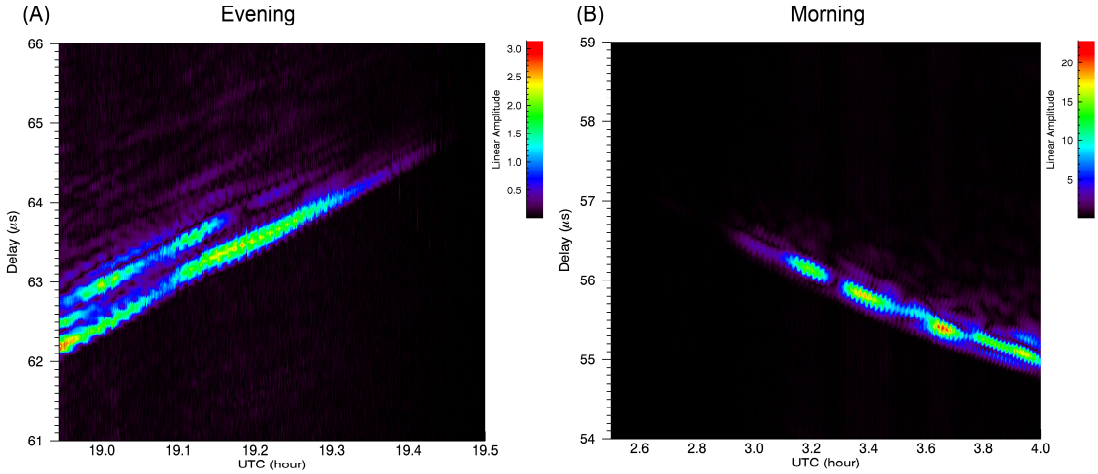


**Fig. S3**

Received signal power detected by CONSERT on Rosetta and plotted with a linear scale (A) during evening hours, and (B) during morning hours of FSS. The vertical axis is the propagation time between Philae and Rosetta and the horizontal axis is the time of measurements.

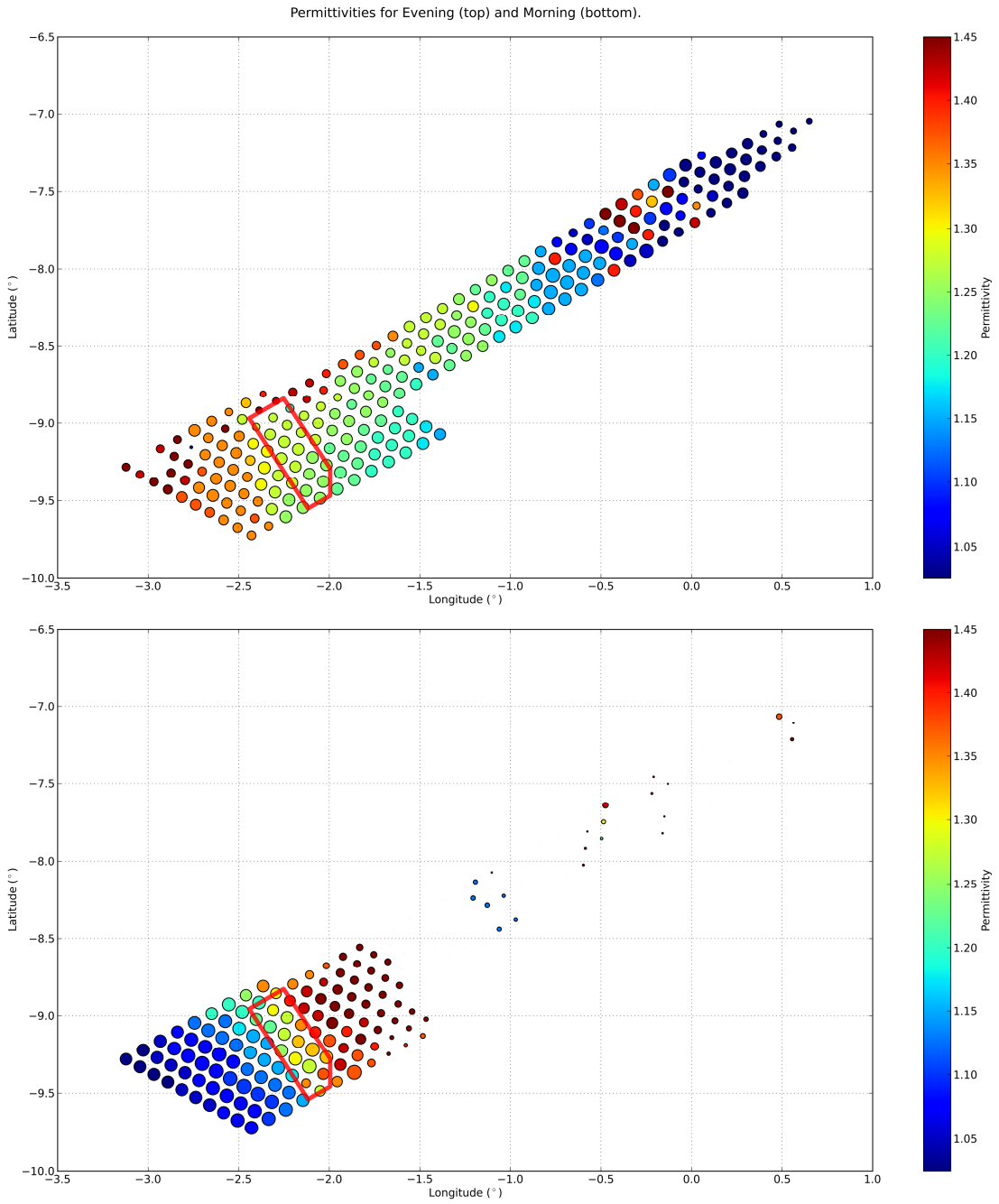


**Fig. S4**

Results from simulation showing the most consistent permittivity values (color) with regard to the measurements, for each possible landing site taken into consideration.
The red bounded area includes landing sites that have the most similar permittivity values in the evening and in the morning.

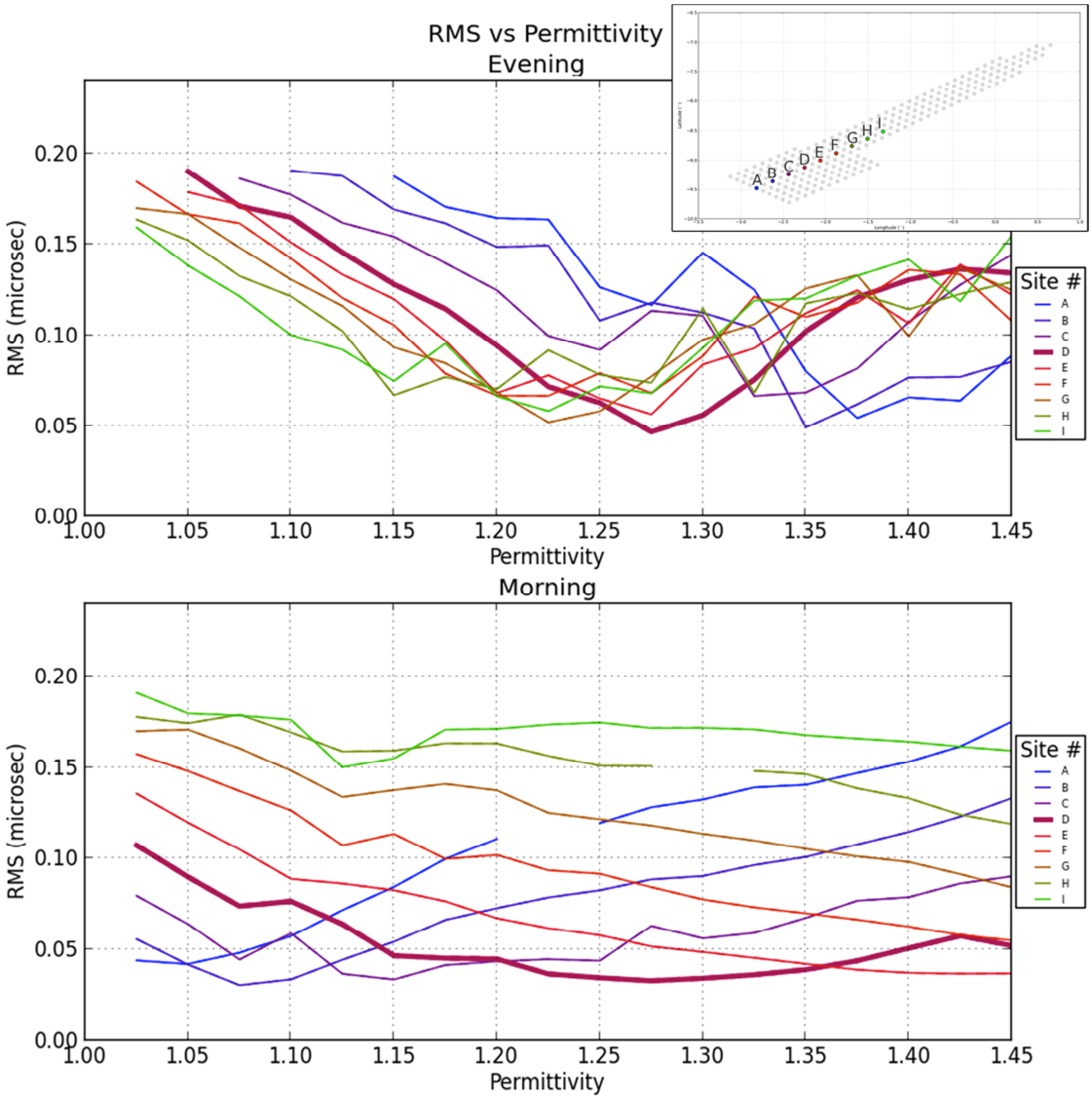


**Fig. S5**

Examples of discrepancy (R.M.S.) between experimental and simulated propagation delays as a function of the assumed dielectric constant value inside the nucleus for a set of 10 potential Philae locations. The upper panel corresponds to the measurements performed during evening and the lower panel during morning.

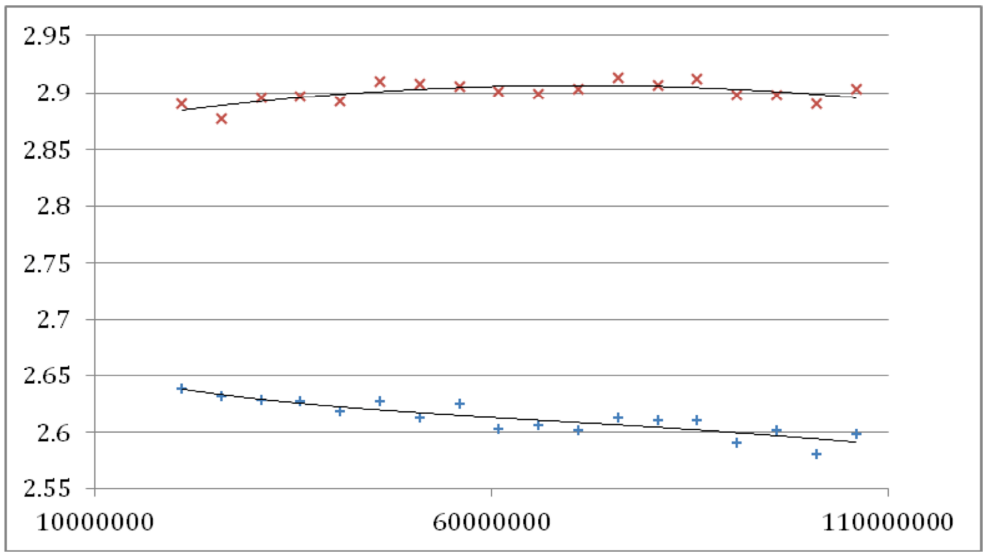


**Fig. S6**

The real part of the dielectric constant for the CR2 (+) and CM2 (x) samples versus frequency (Hz) measured by E. Heggy.

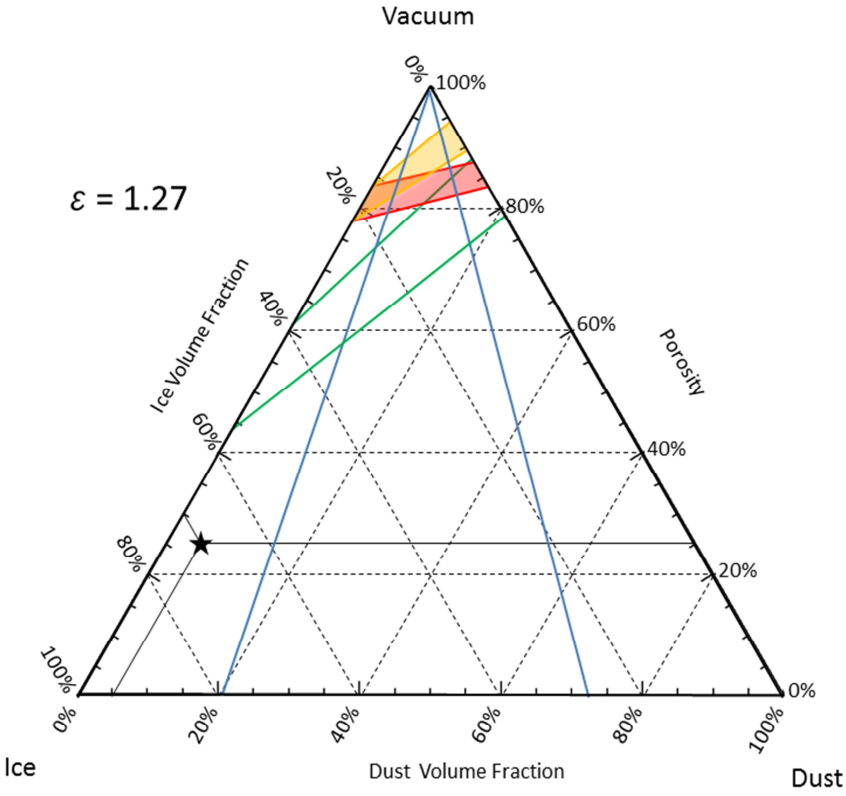


**Fig. S7**

Ternary diagrams for chondrites. To help read this diagram, an example is displayed, star symbol on the figure, corresponding to 25% porosity, 5% dust, and 70% ice.

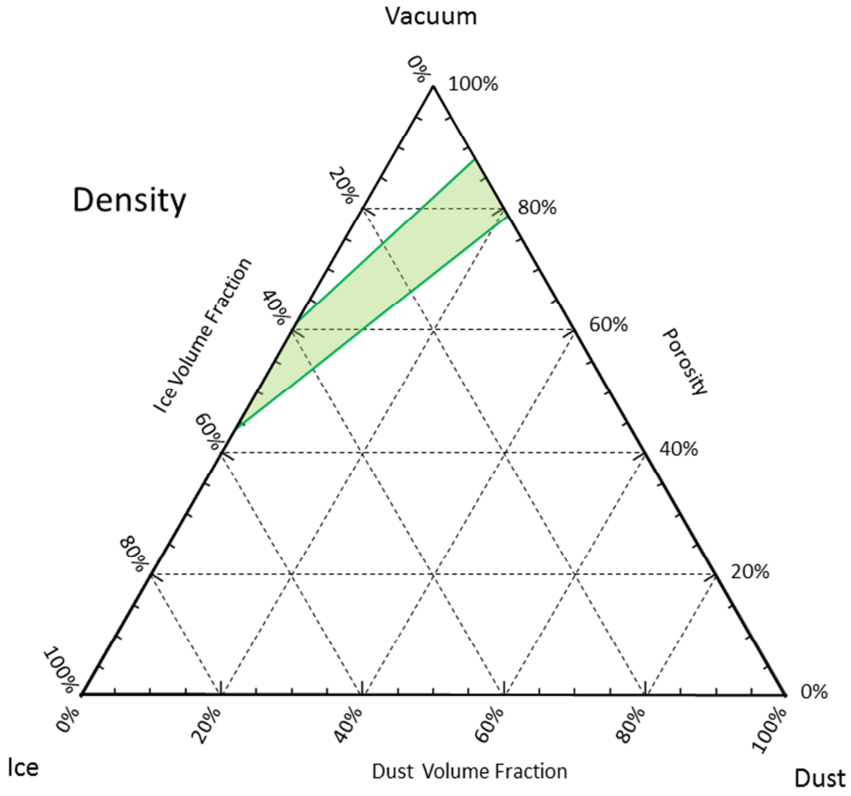


**Fig. S8**
Ternary diagram for the density limits.

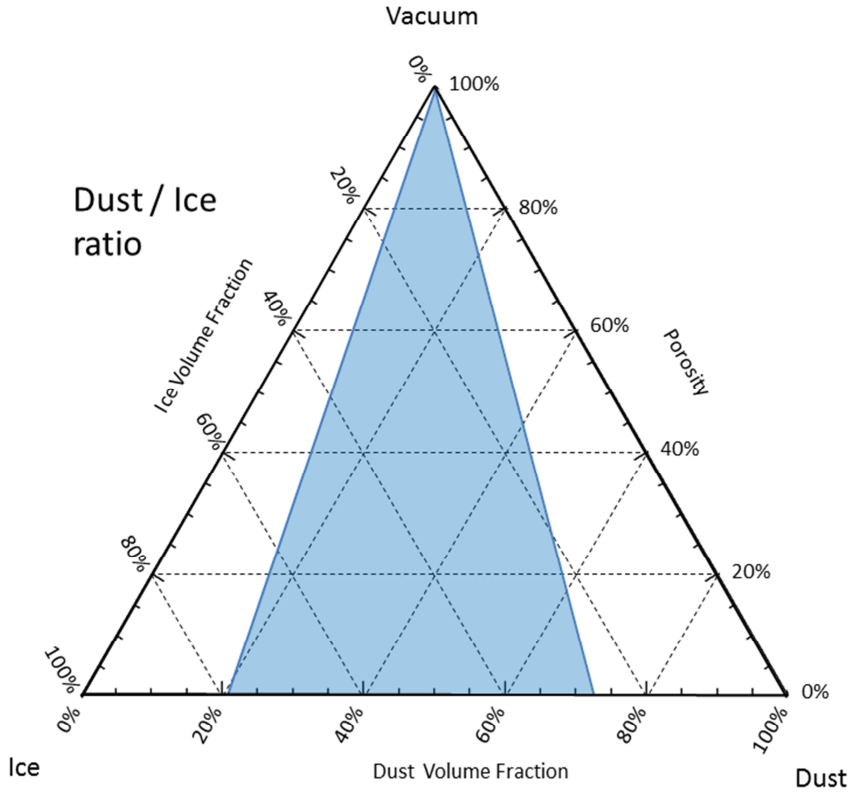


**Fig. S9**
Ternary diagram for assumed Dust to Ice ratio

**Table S1**

Class of quality level for the CONSERT data.

| Table S1 : Class of quality level for the CONSERT data | |
|---|---|
| 1 | Strong SNR with good LCN/OCN synchronization |
| 2 | Positive SNR but no synchronization (RF pollution on LCN) |
| 3 | SNR close to zero (statistical detection of signal) |
| 4 | No signal detection (so far) |

**Table S2**

Quality of the CONSERT data during the FSS.

| Table S2 : Quality of the CONSERT data during the FFS | | | |
|---|---|---|---|
| Signal class | UTC time of beginning | Duration | Period |
| 1 | 12/11/2014 18:56:40 | 00:25:36 | evening |
| 2 | 12/11/2014 19:22:16 | 00:22:44 | |
| 3 | 12/11/2014 19:45:00 | 00:30:00 | |
| 4 | 12/11/2014 20:15:00 | 04:30:00 | |
| 3 | 13/11/2014 00:45:00 | 00:35:00 | |
| 2 | 13/11/2014 01:20:00 | 01:27:02 | |
| 1 | 13/11/2014 02:47:02 | 01:18:42 | morning |

**Table S3**

The materials used and their dielectric properties from Hashin-Shtrikman bounds.
$H_20$ a. stands for amorphous ice.

| Consert | Materials | | Hashin-Shtrikman lower bound | | | | Hashin-Shtrikman upper bound | | | |
|---|---|---|---|---|---|---|---|---|---|---|
| Permittivity | Ice (ε) | Dust Type (ε) | Raw | | Normalized (30%) | | Raw | | Normalized (30%) | |
| | $H_20$ a. (3.4) | - | 15.7% | 84.3% | 15.7% | 84.3% | 11.9% | 88.1% | 11.9% | 88.1% |
| | $H_20$ (3.1) | - | 16.9% | 83.1% | 16.9% | 83.1% | 13.4% | 86.6% | 13.4% | 86.6% |
| | $H_20/CO_2$ (2.8) | - | 18.4% | 81.6% | 18.4% | 81.6% | 15.2% | 84.8% | 15.2% | 84.8% |
| 1.225 | - | C.C. (2.6) | 20.1% | 79.9% | 14.0% | 86.0% | 17.1% | 82.9% | 12.0% | 88.0% |
| | | C.C. (2.9) | 18.0% | 82.0% | 12.6% | 87.4% | 14.7% | 85.3% | 10.3% | 89.7% |
| | - | O.C. (4.7) | 12.6% | 87.4% | 8.8% | 91.2% | 8.1% | 91.9% | 5.6% | 94.4% |
| | | O.C. (5.6) | 11.5% | 88.5% | 8.1% | 91.9% | 6.6% | 93.4% | 4.6% | 95.4% |
| | $H_20$ a. (3.4) | | 18.9% | 81.1% | 18.9% | 81.1% | 14.5% | 85.5% | 14.5% | 85.5% |
| | $H_20$ (3.1) | - | 20.4% | 79.6% | 20.4% | 79.6% | 16.3% | 83.7% | 16.3% | 83.7% |
| | $H_20/CO_2$ (2.8) | - | 22.2% | 77.8% | 22.2% | 77.8% | 18.4% | 81.6% | 18.4% | 81.6% |
| 1.275 | - | C.C. (2.6) | 24.1% | 75.9% | 16.9% | 83.1% | 20.7% | 79.3% | 14.5% | 85.5% |
| | | C.C. (2.9) | 21.7% | 78.3% | 15.2% | 84.8% | 17.8% | 82.2% | 12.5% | 87.5% |
| | - | O.C. (4.7) | 15.2% | 84.8% | 10.6% | 89.4% | 9.8% | 90.2% | 6.9% | 93.1% |
| | | O.C. (5.6) | 13.9% | 86.1% | 9.7% | 90.3% | 8.1% | 91.9% | 5.6% | 94.4% |
| | $H_20$ a. (3.4) | | 22.0% | 78.0% | 22.0% | 78.0% | 17.0% | 83.0% | 17.0% | 83.0% |
| | $H_20$ (3.1) | - | 23.7% | 76.3% | 23.7% | 76.3% | 19.1% | 80.9% | 19.1% | 80.9% |
| | $H_20/CO_2$ (2.8) | - | 25.8% | 74.2% | 25.8% | 74.2% | 21.6% | 78.4% | 21.6% | 78.4% |
| 1.325 | - | C.C. (2.6) | 28.1% | 71.9% | 19.7% | 80.3% | 24.3% | 75.7% | 17.0% | 83.0% |
| | | C.C. (2.9) | 25.2% | 74.8% | 17.6% | 82.4% | 20.9% | 79.1% | 14.6% | 85.4% |
| | - | O.C. (4.7) | 17.7% | 82.3% | 12.4% | 87.6% | 11.5% | 88.5% | 8.1% | 91.9% |
| | | O.C. (5.6) | 16.1% | 83.9% | 11.3% | 88.7% | 9.5% | 90.5% | 6.6% | 93.4% |

**Table S4**

Density as function of measured average density of the comet and assumed grain density, taking into account the errors in density determination.

| Density (kg $m^{-3}$) | Ice density (kg $m^{-3}$) | Dust density (kg $m^{-3}$) | Ice fraction (%) | Dust fraction (%) | Porosity (%) |
|---|---|---|---|---|---|
| 425 | 917 | 3500 | 0.0% | 12.1% | 87.9% |
| | | 2500 | 0.0% | 17.0% | 83.0% |
| | | | 46.3% | 0.0% | 53.7% |
| | 1078 | | 39.4% | 0.0% | 60.6% |
| 515 | 917 | 3500 | 0.0% | 14.7% | 85.3% |
| | | 2500 | 0.0% | 20.6% | 79.4% |
| | | | 56.2% | 0.0% | 43.8% |
| | 1078 | | 47.8% | 0.0% | 52.2% |

**Table S5**

Dust densities and dust/ice mass and volume ratios

| Ice (density) | Dust (density) | Dust/ice mass | Dust/ice vol | Dust/(ice+dust) vol fraction % |
|---|---|---|---|---|
| 917 | 3500 | 1 | 0.26 | 20.8% |
| 917 | 2500 | 1 | 0.37 | 26.8% |
| 1078 | 3500 | 1 | 0.31 | 23.5% |
| 1078 | 2500 | 1 | 0.43 | 30.1% |
| 917 | 3500 | 2 | 0.52 | 34.4% |
| 917 | 2500 | 2 | 0.73 | 42.3% |
| 1078 | 3500 | 2 | 0.62 | 38.1% |
| 1078 | 2500 | 2 | 0.86 | 46.3% |
| 917 | 3500 | 4 | 1.05 | 51.2% |
| 917 | 2500 | 4 | 1.47 | 59.5% |
| 1078 | 3500 | 4 | 1.23 | 55.2% |
| 1078 | 2500 | 4 | 1.72 | 63.3% |
| 917 | 3500 | 6 | 1.57 | 61.1% |
| 917 | 2500 | 6 | 2.20 | 68.8% |
| 1078 | 3500 | 6 | 1.85 | 64.9% |
| 1078 | 2500 | 6 | 2.59 | 72.1% |